Frontiers in Bioscience Landmark

Front. Biosci. (Landmark Ed) **2026**; 31(1): 47597
https://doi.org/10.31083/FBL47597

Original Research

Long Non-Coding RNA *RAB11B-AS1* Suppresses Cervical Cancer Progression by Upregulating *RPL26* Expression

Xuemin Gu[1], Yuanyuan Yang[1], Zhixia Zhang[1], Yiqin Ouyang[2,*], Xiaowen Tong[1,*]

[1]Department of Obstetrics and Gynaecology, Shanghai Tongji Hospital of Tongji University, Tongji University School of Medicine, 200065 Shanghai, China
[2]Department of Obstetrics and Gynaecology, Shanghai Dongfang Hospital of Tongji University, Tongji University School of Medicine, 200065 Shanghai, China
*Correspondence: oyyq1124@hotmail.com (Yiqin Ouyang); tongxiaowen2022@163.com (Xiaowen Tong)
Academic Editors: Giovanni Tossetta and Amancio Carnero Moya
Submitted: 22 October 2025 Revised: 27 November 2025 Accepted: 15 December 2025 Published: 16 January 2026

Abstract

Background: Cervical cancer (CC) is one of the most prevalent gynecological malignancies. The expression and functional role of the long non-coding RNA (*lncRNA*) *Ras-related protein Rab-11B antisense RNA 1* (*RAB11B-AS1*) in CC remain poorly understood. **Methods**: The expression profile of lncRNA *RAB11B-AS1* across multiple cancer types was initially assessed using data from The Cancer Genome Atlas. Its expression in CC tissues and lesions of varying pathological grades was subsequently validated via RNA *in situ* hybridization. To investigate its functional role in CC, a combination of transcriptomic, proteomic, and functional assays was employed to delineate the molecular role of *RAB11B-AS1*. The effects of alterations in *RAB11B-AS1* expression on cervical cancer growth were ultimately validated *in vivo*. **Results**: LncRNA *RAB11B-AS1* was downregulated in CC and associated with a favorable patient prognosis. Functionally, *RAB11B-AS1* promoted apoptosis while suppressing proliferation, migration, and invasion of CC cells *in vitro*, and inhibited tumor growth *in vivo*. Mechanistically, *RAB11B-AS1* upregulated ribosomal protein L26 (*RPL26*) expression. Notably, *RAB11B-AS1* suppressed cervical cancer progression by activating the p53 pathway via *RPL26*. Critically, *in vitro* and *in vivo* experiments confirmed that *RPL26* knockdown abrogates the tumor-suppressive functions of *RAB11B-AS1*, establishing *RPL26* as a pivotal downstream effector of *RAB11B-AS1* in CC. **Conclusions**: Our findings demonstrate that lncRNA *RAB11B-AS1* suppresses cervical cancer progression primarily through upregulation of *RPL26* and suggest that *RAB11B-AS1* may serve as a potential biomarker and therapeutic target in cervical cancer.

Keywords: *RAB11B-AS1*; cervical cancer; cell proliferation; metastasis; apoptosis; ribosomal protein L26

1. Introduction

Cervical cancer (CC) is among the most prevalent malignant neoplasms that pose a threat to global women's health [1]. Globally, CC is the fourth most common cancer in women, accounting for an incidence of 6.6% and a mortality rate of 7.5% [2]. Both its morbidity and mortality rates have been on the rise [3]. Despite the comprehensive and diversified diagnostic and treatment approaches for CC, the prognosis for patients with locally advanced or metastatic CC remains very poor [4]. Consequently, foundational molecular research into CC progression may lead to the identification of novel therapeutic targets.

Long non-coding RNAs (lncRNAs) have gained increasing recognition in cancer biology as pivotal regulators of gene expression. Numerous studies have established that lncRNAs play fundamental roles as oncogenes or tumor suppressors, governing key aspects of tumorigenesis such as cell proliferation, apoptosis, invasion, and metastasis, through their involvement in chromatin remodeling, transcription, and post-transcriptional modifications [5]. In cervical cancer, several lncRNAs (e.g., *MALAT1*, *PVT1*) have been mechanistically implicated in proliferation, metastasis, therapy resistance and immune modulation, underscoring the central role of lncRNAs in disease biology and their potential as diagnostic or therapeutic targets [6].

The lnc-RNA Ras-related protein Rab-11B antisense RNA 1 (*RAB11B-AS1*) is transcribed from the opposite strand of the RAB11B gene transcription, which contains 1034 nucleotides (three exons) and is located at chromosomal band 19p13.2 [7]. Existing studies have reported its involvement in tumorigenesis across various cancer types, yet its functions are highly context-dependent. *RAB11B-AS1* is downregulated in osteosarcoma but shows elevated expression in lung and breast cancers [8–10]. Notably, in breast cancer, it enhances the expression of pro-angiogenic factors *VEGFA* and *ANGPTL4*, thereby promoting cell migration and invasion [10]. Furthermore, a recent study revealed that *METTL16* diminishes *RAB11B-AS1* stability via m6A modification, leading to its downregulation, which subsequently suppresses proliferation, migration, and invasion while promoting apoptosis in hepatocellular carcinoma (HCC) cells [11]. However, the functional role and underlying molecular mechanism of *RAB11B-AS1* in CC have not been fully investigated. Because lncRNAs often function as upstream

modulators of oncogenic signaling and exhibit high tissue specificity, dissecting the mechanistic role of *RAB11B-AS1* may not only fill an important gap in cervical cancer biology but also reveal new avenues for therapeutic development.

In this study, tumorigenesis tests were conducted *in vitro* and *in vivo* to analyze the effect of *RAB11B-AS1* on CC. The results revealed that *RAB11B-AS1* is negatively associated with pathological grade in human CC and inhibits the growth of CC cells via the ribosomal protein L26 (RPL26)-p53 axis. These results shed light on a new prospect for CC therapy development.

2. Materials and Methods

2.1 Bioinformatics Analysis

The expression of lnc-RNA *RAB11B-AS1* was analyzed using data from the TCGA database (https://cancergenome.nih.gov/) and data regarding *RAB11B-AS1* copy number alterations were sourced from cBioPortal (https://www.cbioportal.org/). The Kaplan-Meier survival analysis was employed to assess the overall survival of patients diagnosed with cervical cancer, with a *p*-value of less than 0.05 being defined as statistically significant.

2.2 Specimens

A total of 135 formalin-fixed, paraffin-embedded (FFPE) cervical tissue specimens were included in this study, which were collected from patients in our hospital between January 2019 and June 2024. The cohort consisted of two groups: 35 adjacent non-cancerous tissue specimens and 100 cervical carcinoma tissue specimens. The adjacent normal tissues were obtained from the non-cancerous periphery of surgical resections in patients with early-stage cervical cancer, all of which were confirmed to be histologically normal by pathological examination. The carcinoma tissues were collected from patients who underwent biopsy or surgical procedures in our Department of Gynecology, with a confirmed diagnosis of cervical cancer. All tissue specimens were processed according to standard protocols within 30 minutes after resection, fixed in 10% neutral buffered formalin, routinely embedded in paraffin, and stored in our hospital's pathology department biobank for subsequent sectioning and analysis. All cervical cancer patients enrolled in this study were treated at the Department of Obstetrics and Gynecology, Shanghai Tongji Hospital. None of the included patients had a history of other malignant tumors, and 135 patients not undergone any radio or chemotherapy prior to this study. This study was conducted in accordance with the guiding principles of the Declaration of Helsinki. The experimental protocol was approved by the Ethics Committee of Shanghai Tongji Hospital (Approval Number: K-W-2025-011), and prior written informed consent was acquired from all enrolled patients.

2.3 Cell Line

The human cervical carcinoma cell line SiHa was commercially purchased from the American Type Culture Collection (ATCC) (Catalog No. HTB-35) and was cultured strictly according to the provider's guidelines. SiHa was cultured at 37 °C in 90% humidity and 5% carbon dioxide (CO_2) in DMEM medium (Gibco, Thermo Fisher Scientific, Waltham, MA, USA) with 10% fetal bovine serum (FBS) (Gibco, USA) and penicillin-streptomycin (Gibco, Thermo Fisher Scientific, Waltham, MA, USA) in a CO_2 incubator. All cell lines were validated by short tandem repeat analysis and tested negative for mycoplasma.

2.4 In Situ Hybridization

The expression of *RAB11B-AS1* was detected using RNAscope, a novel RNA *in situ* hybridization assay. Specific RNAscope probes targeting *RAB11B-AS1* (Probe-Hs-*RAB11B-AS1*, Cat # 838261, Advanced Cell Diagnostics, Newark, CA, USA) were employed. *RAB11B-AS1* expression levels were quantified using the semiquantitative histopathological ACD scoring system, which is outlined below: Zero = no staining or fewer than one red punctate dot per ten cells; one = one to three dots per cell; two = four to nine dots per cell with no or rare clustering; three = ten to fifteen dots per cell and/or fewer than ten per cent of dots in clusters; four = at least fifteen dots per cell and/or at least ten per cent of dots in clusters.

2.5 RNA Extraction and qRT-PCR

Total RNA extraction was carried out using Trizol reagent (Cat. No. F419KA1560, Sangon Biotech, Shanghai, China) according to the manual. The reverse transcription process was carried out utilising the PrimeScript RT Reagent Kit (Cat. No. RR047A, Takara Bio, Tokyo, Japan). Quantitative PCR (qPCR) was conducted using PrimeSTAR Max DNA Polymerase with SYBR Green (Cat. No. R045A, Takara Bio, Tokyo, Japan) on an ABI7500 instrument (This product was manufactured by Applied Biosystems, a company based in Carlsbad, CA, USA).

All primer sequences were synthesized by Shanghai Sangon Biological Co., LTD. The specific sequences are as follows:

RAB11B-AS1 forward (5′-3′): TAATCCCAGCCATTTGTG,

RAB11B-AS1 reverse (5′-3′): GAATCTCGCTCTGTTGCC.

RPL26 forward (5′-3′): GACAGAAGTACAACGTGCGA,

RPL26 reverse (5′-3′): TTTTGCGGTCTTTGTCCAGT.

β-actin forward (5′-3′): CCCTGGAGAAGAGCTACGAG,

β-actin reverse (5′-3′): CGTACAGGTCTTTGCGGATG).

β-actin was set as the internal reference gene for other transcripts. The $2^{-\Delta Ct}$ method (ΔCt = Ct target gene – Ct internal reference) was used to calculate the relative mRNA expression of each target gene.

2.6 Plasmid Construction, Lentivirus Preparation and Infection

The full-length cDNA of human *RAB11B-AS1* (NR_038237.1) was synthesized by Viral Therapy Technologies (Wuhan, China) and was cloned into lentiviral vector pLVX-ZsGreen-Puro. rLV-CON and rLV-*RAB11B-AS1* were prepared with pLVX-ZsGreen-Puro and pLVX-*RAB11B-AS1*-ZsGreen-Puro, respectively (Viral Therapy Technologies, Wuhan, China).

The *RAB11B-AS1* sgRNA targeting RAB11B-AS1 (5′-GGCTAGGATGCGCGGCTATACGG-3′) was cloned into the lentiviral vector pLVX-U6-CMV-Cas9-P2A-ZsGreen to construct recombinant plasmid pLVX-U6-*RAB11B-AS1* sgRNA-Cas9-ZsGreen (pLVX-Cas9-*RAB11B-AS1*). The resulting plasmid, which was used to produce the lentiviruses rLV-Cas9-*RAB11B-AS1*, rLV-Cas9-CON and rLV-Cas9-*RAB11B-AS1*, was prepared by Viral Therapy Technologies (Wuhan, China). The infection of SiHa cells with rLV-Cas9-CON and rLV-Cas9-RAB11B-AS1 was conducted in strict accordance with the manufacturer's guidelines.

The sh*RPL26* (5′-GAAGTACAACGTGCGATCCAT-3′) was cloned into the pLVX-shRNA-mCherry-hygro (lentiviral vector) to construct a plasmid pLVX-shRNA-mCherry-hygro to construct a recombinant plasmid pLVX-shRNA-mCherry-hygro-h*RPL26* (pLVX-*RAB11B-AS1*-si*RPL26*) which was then packaged into a lentivirus rLV-*RAB11B-AS1*+ rLV-shRNA-*RPL26*. Next, the infection of SiHa cells with rLV-CON, rLV-*RAB11B-AS1*, rLV-*RAB11B-AS1*+ rLV-shRNA-*RPL26*.

2.7 Cell Viability Assay

The SiHa cells were seeded 2×10^3 cells per well in a 96-well plate. Optical density at 450 nm (OD450) was measured using CCK-8 reagents (MCE, Sigma-Aldrich, St. Louis, MO, USA) at different time points (0 h, 24 h, 48 h, 72 h, 96 h) according to manufacturer instructions. Cell proliferation ability was determined according to OD450.

2.8 Plate Colony Formation Assays

A total 600 cells were seeded in a 6-well culture dish and subsequently cultured for a period of two weeks. The colonies were fixed with methanol for a period of 15 minutes and subsequently stained with 0.5% Giemsa for a further 10 minutes. The colonies were observed and enumerated.

2.9 Cell Apoptosis Assay

The SiHa cell apoptosis was detected using the AnnexinV-APC/7-AAD Apoptosis Detection Kit (Tianjin Sungene Biotech Co., Ltd., Tianjin, China). Briefly, cells were stained with 7-AAD (5 µL) and Annexin V-APC 1 µL in the dark for 15 min. Then the cells were detected using a flow cytometer (CytoFLEX, Beckman Coulter Life Sciences, Brea, CA, USA).

2.10 Cell Migration and Invasion Assays

Cells were seeded into upper transwell chambers (Lot: 353097; Corning Inc., Corning, NY, USA) coated with or without Matrigel at a density of 6×10^4 cells in 200 µL serum-free medium; 600 µL medium containing 10% FBS was added to the lower chambers. Following a 24 h incubation period, the cells located on the lower membrane were subjected to fixation in 70% ethanol at 4 °C for 1 h and then stained with 0.5% methylrosanilinium chloride solution for at least 20 min. Migrated and invaded cells were visualized under a microscope (200×).

2.11 Western Blot

1.2×10^6 SiHa cells were lysed by RIPA lysis buffer containing PMSF (Beyotime, Shanghai, China). Approximately 15 µg of protein extracts were separated with a precast BeyoGel™ SDS-PAGE gel (Beyotime, Shanghai), transferred onto nitrocellulose membranes, and probed with primary antibodies (anti-*RPL26*, 1:1000, ab59567, Abcam, Cambridge, UK; GAPDH, 1:10,000, 60004-1-Ig, Proteintech Group, Wuhan, China). Membranes were incubated at 4 °C for 24 h, then with HRP-conjugated secondary antibodies (HRP-labeled Goat Anti-Rabbit IgG (H+L), 1:1000, A0208, Abclonal, Wuhan, China) for 2 h at room. The proteins were visualized by enhanced chemiluminescence.

2.12 EdU Assay

SiHa cells were seeded in a 24-well plate at a density of 5×10^4 cells per well and cultured for 24 hours in a humidified incubator at 37 °C with 5% CO_2. Each well received 100 µL of the EdU-containing medium. The plate pulsed for 2 hours. Following the wash steps, the cells were permeabilized and processed for the click chemistry reaction, as per the kit protocol, to fluorescently label the incorporated EdU. This was followed by nuclear counterstaining. The samples were visualized and imaged using a fluorescence microscope. The percentage of EdU-positive cells was quantified by analyzing the acquired images with ImageJ software.

2.13 RNA-Sequencing Analysis

Total cellular RNA was extracted in accordance with the manufacturer's instructions. Construction of the sequencing library and RNA-sequencing (RNA-seq) were performed by Beijing Novogene Company.

2.14 Protein Tandem Mass Tag Analysis

The total proteins were isolated. In brief, the samples were lysed with a 0.5 mL lysis buffer, which contains 6 M

Urea, 0.1 M ammonium bicarbonate, and 0.2% SDS. Extracts were reduced with 10 mM DTT for 1 h at 56 ℃ and subsequently alkylated with sufficient iodoacetamide for 1 h at room temperature shielded from light. Then samples were mixed with 4 times the volume of precooled acetone by vortexing and incubated at –20 ℃ for at least 2 h. Subsequently, the samples were subjected to a process of centrifugation, resulting in the collection of the precipitation. Following two cycles of washing with cold acetone, dissolution of the pellet was achieved by means of dissolution buffer. This buffer contains 0.1 M triethylammonium bicarbonate (TEAB, pH 8.5) and 6 M urea. LC–MS/MS analyses were performed in Beijing Novogene Company.

2.15 Chromatin Immunoprecipitation Sequencing Analysis

A total of 3×10^7 cells from the rLV-*RAB11B-AS1* group and rLV-CON group were processed using PIS (Novogene Company, Beijing, China) and PMSF (Beyotime, Shanghai). Cells were fixed in 1% formaldehyde for 10 minutes, and the fixation was quenched by adding 0.125 M glycine for 5 min. Chromatin immunoprecipitation sequencing (ChIP-seq) for histone H3 lysine 9 acetylation (H3K9Ac) was performed by Beijing Novogene Company.

2.16 Tumorigenesis Test In Vivo

Female BALB/c nude mice aged between four and six weeks were procured from Shanghai JieSiJie Laboratory Animal Co., Ltd. The housing of the mice was conducted in accordance with the guidelines stipulated by the National Institutes of Health (NIH) Guide for the Care and Use of Laboratory Animals (NIH Publication No. 8023, revised 1978). It is imperative to note that all procedures conducted in an animal experimental context were meticulously reviewed and formally endorsed by the esteemed Animal Ethics Committee of Tongji University (Approval Number: TJAB04225102).

SiHa cells in the logarithmic growth phase were digested with trypsin, resuspended in phosphate-buffered saline (PBS), and counted to achieve a final concentration of 5×10^6 cells per mouse. A 50 µL aliquot of the cell suspension was mixed with an equal volume of Matrigel on ice. The mixture was loaded into a 1 mL syringe and injected subcutaneously into the left axilla of each mouse to construct a nude mouse xenograft model. Following injection, the mice were returned to a specific pathogen-free (SPF) environment and maintained under standard conditions. Once tumors grew to about 150–200 mm^3 in size following a 30-day period, the mice were humanely euthanized via rapid anesthesia induced by 5% isoflurane in an induction chamber. The resulting tumors were excised, photographed, and weighed. Some tumor samples were fixed in formalin for subsequent immunohistochemical analysis.

2.17 Statistical Analysis

Statistical analysis was performed using SPSS 22.0 software (IBM Corp, SPSS, Chicago, IL, USA) and GraphPad Prism software (Version 8.0.2, GraphPad Software, Inc., San Diego, CA, USA). The measurement data were expressed as the mean ± standard deviation (S.D.). The significance of differences between groups was estimated by two-tailed student's *t*-tests, one-way ANOVA and Wilcoxon rank sum test. A *p*-value of less than 0.05 was considered to be significant. *, $p \leq 0.05$; **, $p \leq 0.01$; ***, $p \leq 0.001$; ****, $p \leq 0.0001$; ns, not statisticant.

3. Results

3.1 RAB11B-AS1 Upregulation Correlates With Better CC Prognosis

In order to investigate the association between RAB11B-AS1 and cancers, the TCGA data was analysed initially. The study revealed a substantial decrease in RAB11B-AS1 expression levels in tumor tissues compared to normal tissues across the majority of cancer types (Fig. 1A). Concurrent analysis using cBioPortal indicated copy number loss of *RAB11B-AS1* in 82% of CC cases (Fig. 1B). Consequently, we assessed *RAB11B-AS1* expression in normal cervical tissues and CC tissues using RNA *in situ* hybridization. The results demonstrated significant downregulation of *RAB11B-AS1* in cervical cancer tissues, with markedly lower RNAscope scores compared to normal tissues (Fig. 1C,D). Further analyses across different histological grades revealed a progressive decline in *RAB11B-AS1* expression with increasing tumor grade, reaching its lowest level in grade 3 (G3) CC (Fig. 1E,F). In conclusion, the analysis of online survival curves demonstrated that patients exhibiting elevated levels of RAB11B-AS1 expression demonstrated a more favorable prognosis (Fig. 1G).

3.2 RAB11B-AS1 Inhibits the Tumorigenic Cervical Cancer Cells In Vitro

To explore the functional role of RAB11B-AS1 in cervical cancer, we generated SiHa cell lines with stable overexpression of RAB11B-AS1. As shown in Fig. 2A, RAB11B-AS1 expression was significantly higher in rLV-RAB11B-AS1 cells than in rLV-CON control cells. Subsequent CCK-8 assays revealed that overexpression of RAB11B-AS1 significantly inhibited the proliferation of SiHa cells (Fig. 2B). Consistent with this, colony formation assays revealed that RAB11B-AS1-overexpressing cells formed significantly fewer colonies than controls (Fig. 2C). Further analysis using Transwell assays showed that SiHa cells with RAB11B-AS1 overexpression exhibited significantly impaired migratory and invasive capacities (Fig. 2D,E). To corroborate the anti-proliferative effect, EdU incorporation assays were performed, confirming significantly attenuated proliferation in rLV-*RAB11B-AS1* cells versus rLV-CON cells (Fig. 2F). Finally, flow cytometric

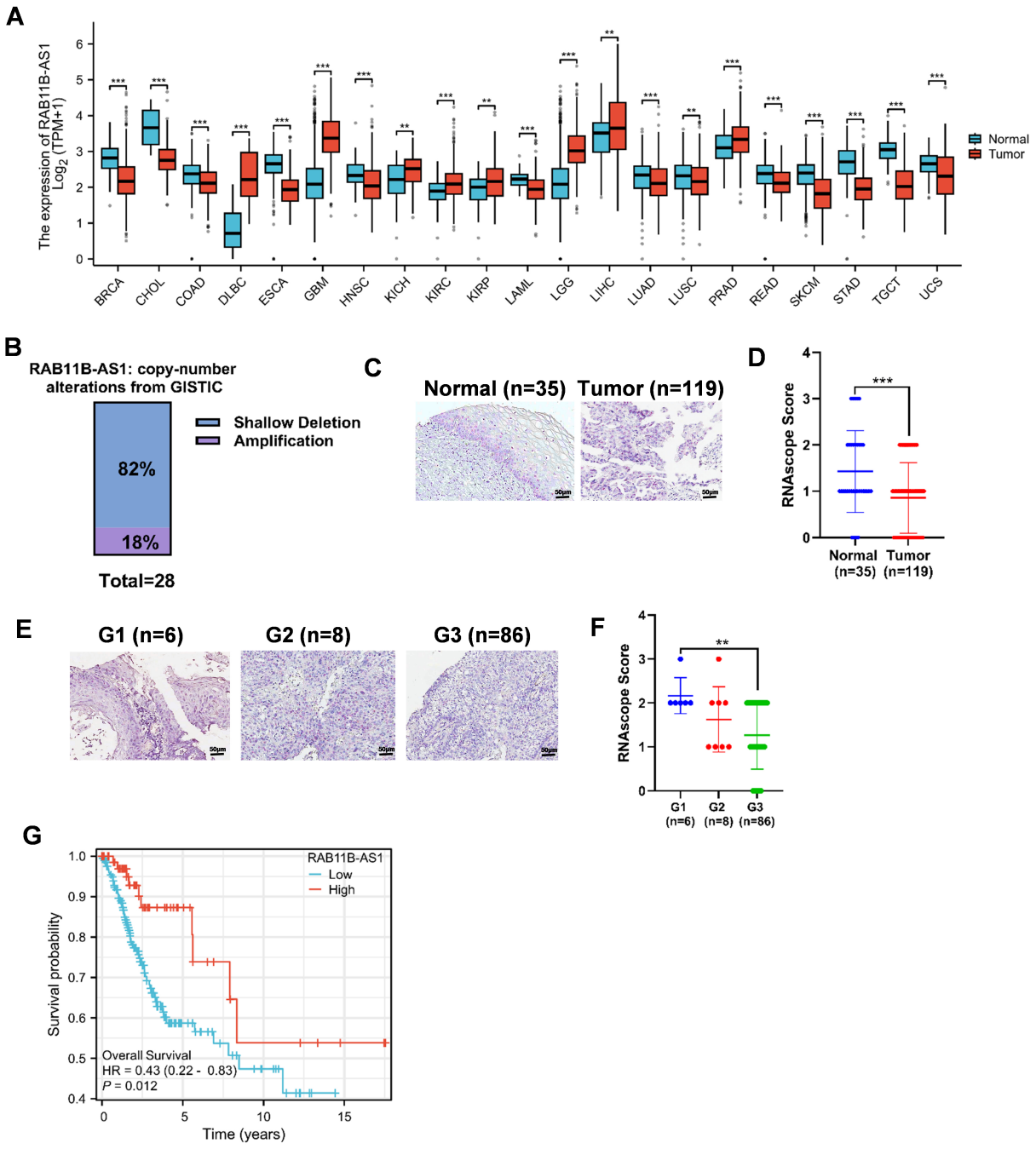

Fig. 1. RAB11B-AS1 upregulation correlates with better CC prognosis. (A) RAB11B-AS1 expression in normal and cancer tissues of multiple cancers via TCGA data. (B) Copy number variation of RAB11B-AS1 in CC in the cBioPortal database (https://www.cbioportal.org/). (C) Expression level of RAB11B-AS1 in 35 normal cervical tissues and 100 CC tissues. All micrographs (20×; scale bar, 50 μm). (D) RNAscope Scores of RAB11B-AS1 in CC and normal cervical tissues. Measurement data are expressed as the mean ± SD. (E) Expression of RAB11B-AS1 in G1, G2, and G3 CC by *in situ* hybridization staining. All micrographs (20×; scale bar, 50 μm). (F) Analysis of RAB11B-AS1 expression in G1, G2, and G3 CC. The measurement data were expressed as the mean ± SD. CC is categorized as follows: (G1) Carcinoma of the cervix that exhibits significant heterogeneity. (G2) moderately differentiated CC. (G3) poorly differentiated CC. (G) Prognostic analysis of patients with CC with high and low RAB11B-AS1 expression in online data using Kaplan-Meier curves. For (A) statistical analyses were performed using Wilcoxon rank sum test. For (D,F) Data represent the mean ± SD, and statistical analyses were performed using two-tailed unpaired *t*-tests. RAB11B-AS1, Ras-related protein Rab-11B antisense RNA 1; CC, Cervical cancer; TCGA, The Cancer Genome Atlas; SD, standard deviation. **, $p \leq 0.01$; ***, $p \leq 0.001$.

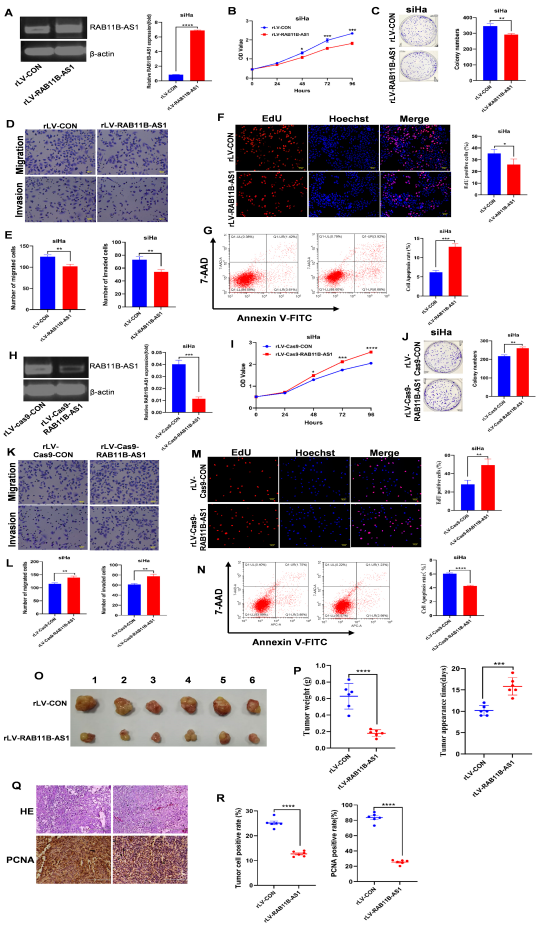

Fig. 2. *RAB11B-AS1* inhibits the tumorigenic cervical cancer cells *in vitro*. (A) RT-qPCR detected *RAB11B-AS1* in SiHa cells infected with either rLV-CON or rLV-*RAB11B-AS1*. (B) CCK-8 assay was used to determine the impact of *RAB11B-AS1* overexpression on SiHa cell proliferation. (C) The ability of cell colonies to form was compared between the rLV-*RAB11B-AS1* group and the rLV-CON group. Representative images from three independent biological replicates are shown. (D,E) Pictures show cell migration and invasion in SiHa cells infected with rLV-CON and rLV-*RAB11B-AS1*. Cell migration is shown in the upper panel and cell invasion in the lower panel. All micrographs are ×20 magnification with a scale bar of 50 μm. Representative images from three independent biological replicates are shown. (F) EdU assay was used to detect the cell proliferation ability of *RAB11B-AS1* in the rLV-CON group and rLV-*RAB11B-AS1* group. All micrographs (20×; scale bar, 50 μm). Representative images from three independent biological replicates are shown. (G) Detection of apoptosis in SiHa cells infected with rLV-CON and rLV-*RAB11B-AS1* by Annexin V-APC/7-AAD staining on flow cytometer. Representative images from three independent biological replicates are shown. (H) *RAB11B-AS1* knockdown efficiency was determined by PCR gel electrophoresis and qRT-PCR. (I) CCK-8 assay was used to detect the effect of *RAB11B-AS1* knockout on the proliferation of SiHa cells. (J) Ability of cell colonies to form was compared in the rLV-Cas9-*RAB11B-AS1* group and the rLV-Cas9-CON group. Representative images from three independent biological replicates are shown. (K,L) Cell migration and invasion assays were performed on SiHa cells infected with rLV-Cas9-CON and rLV-Cas9-*RAB11B-AS1*. All micrographs (20×; scale bar, 50 μm). Representative images from three independent biological replicates are shown. (M) The impact of *RAB11B-AS1* knockout on SiHa cell proliferation was evaluated using an EdU incorporation assay. All micrographs (20×; scale bar, 50 μm). Representative images from three independent biological replicates are shown. (N) Flow cytometry was used to evaluate the apoptotic rate in SiHa cells following *RAB11B-AS1* knockout. Representative images from three independent biological replicates are shown. (O) Nude mice were euthanized after 30 days, and the transplanted tumors were imaged. (P) Comparison of average xenograft tumor weight and appearance time (days) between the rLV-*RAB11B-AS1* and rLV-CON group. (Q) H&E staining and immunohistochemistry with anti-PCNA from xenograft tumors between rLV-*RAB11B-AS1* and rLV-CON (scale bar, 200 μm). (R) Analysis of the H&E staining cell positive rate (%) and PCNA positive rate (%) from xenograft tumor between rLV-*RAB11B-AS1* and rLV-CON groups. All measurement data are expressed as the mean ± SD. For (A,C,E–H,J,L–N,P,R) Data represent the mean ± s.d., and statistical analyses were performed using two-tailed unpaired *t*-tests. For (B,I) statistical analyses were performed using one-way ANOVA tests. *, $p \leq 0.05$; **, $p \leq 0.01$; ***, $p \leq 0.001$; ****, $p \leq 0.0001$.

analysis indicated that *RAB11B-AS1* overexpression significantly increased the apoptosis rate in SiHa cells (Fig. 2G).

To further validate the inhibitory role of *RAB11B-AS1* in CC cells, we used CRISPR-Cas9 technology to generate RAB11B-AS1 knockout SiHa cells. The efficiency of the knockout was confirmed by qRT-PCR and PCR gel electrophoresis (Fig. 2H). Subsequent functional assays revealed that *RAB11B-AS1* depletion significantly enhanced the proliferative capacity of SiHa cells and increased colony formation compared to control cells (Fig. 2I,J). Furthermore, *RAB11B-AS1* knockout markedly promoted cell migration and invasion relative to the rLV-Cas9-CON control group (Fig. 2K,L). EdU incorporation assays corroborated the enhanced proliferation upon *RAB11B-AS1* loss (Fig. 2M). Finally, flow cytometry demonstrated a significant reduction in apoptosis in *RAB11B-AS1* knockout cells compared to controls (Fig. 2N). Taken together, these results demonstrate that RAB11B-AS1 suppresses the proliferation, migration and invasion of cervical cancer cells *in vitro*, while promoting apoptosis.

Consequently, we evaluated its function *in vivo* using a xenograft tumor model in nude mice. Tumors derived from rLV-*RAB11B-AS1* cells exhibited significantly smaller volumes, reduced average weight, and delayed onset compared to tumors from rLV-CON control cells (Fig. 2O,P). Histological analysis (H&E staining) revealed a significant reduction in the number of poorly differentiated cells in rLV-RAB11B-AS1 tumors compared to the control group (Fig. 2Q). Further immunohistochemical analysis revealed significantly lower PCNA positivity in the rLV-RAB11B-AS1 group than in the rLV-CON group (Fig. 2R). Overall, these results suggest that RAB11B-AS1 inhibits cervical tumor growth.

3.3 RAB11B-AS1 Enhances the Transcriptional Activity of RPL26 by Altering the Modification of H3K9Ac

As *RAB11B-AS1* has been shown to inhibit the growth of human cervical cancer cells *in vitro* and *in vivo*, it is important to identify the genes and signaling pathways affected by *RAB11B-AS1* in cervical tumor development. First, we performed chromatin immunoprecipitation sequencing (ChIP-seq) with anti-H3K9Ac in the two stable cell lines (Fig. 3A). Heat map analysis showed 16496 up peaks and 475 down peaks, such as *RPL26*, *S100A14*, echinoderm microtubule-associated protein like 2 (EML2), cellular retinoic acid-binding protein 2 (CRABP2), microtubule-associated protein 2 (MAP2), RPL35, RPL37, RPL28, and CDC28 protein kinase regulatory subunit 1B (CKS1B) (Fig. 3B). KEGG enrichment analysis of differentially expressed genes revealed the primary cellular pathways affected by the overexpression of *RAB11B-AS1*. Genes found to be downregulated following this overexpression—specifically those identified via ChIP-seq peak analysis—were significantly associated with several key biological processes, particularly ribosome, regulation of actin cytoskeleton, neuroactive ligand-receptor interaction, focal adhesion, and axon guidance (Fig. 3C). Further analyses revealed a difference in the modification ability of H3K9Ac on chromosome 17: the rLV-CON group contained 1500 peaks, whereas the rLV-*RAB11B-AS1* group contained 3311 peaks. Moreover, the modification ability of H3K9Ac in the promoter regions of several genes was different. For example, six peaks appeared in the promoter region of *RPL26* in the rLV-*RAB11B-AS1* group and three peaks appeared in the rLV-CON group (Fig. 3D). Compared with the rLV-CON group, the scores of peaks in *RPL26* were higher than those in the rLV-*RAB11B-AS1* group (Fig. 3E). The pGL3-*RPL26*-promoter-LUC luciferase reporter gene with the *RPL26* promoter sequence was transfected into two groups of cells (rLV-CON and rLV-*RAB11B-AS1*). The results showed that, compared with the rLV-CON group, luciferase reporter gene activity was significantly higher in the rLV-*RAB11B-AS1* group (Fig. 3F). Taken together, these results suggest that *RAB11B-AS1* increases H3K9Ac modification in the RPL26 promoter region.

We sought to identify how *RAB11B-AS1* affected on some genes and related signaling pathways involved in cervical tumorigenesis. Firstly, we analyzed transcriptome by RNA sequencing in the two stable cell lines. The results show that 19,605 differentially expressed transcripts were identified among the 133,924 transcripts analysed, including 9498 transcripts that were up-regulated and 10,107 transcripts that were down-regulated in the rLV-*RAB11B-AS1* group compared to the rLV-CON group (Fig. 3G). In particular, the expression of RPL26 was significantly higher in the rLV-*RAB11B-AS1* group than in the rLV-CON group (Fig. 3G). Transcriptome GO analysis revealed that, compared to the rLV-CON group, the rLV-*RAB11B-AS1* group showed significant enrichment of gene sets in pathways related to chipmaker perception, substrate-specific channel activity, plasma membrane protein complex, passive transmembrane transporter activity, ion channel activity, and channel activity (Fig. 3H). KEGG analysis showed that the differential transcripts were highly enriched in pathways related to the neuroactive ligand-receptor interaction, calcium signaling pathway, and cell adhesion molecules (CAMs) (Fig. 3I). Reactome analysis revealed the substantial enrichment of differential transcripts in the rLV-*RAB11B-AS1* group than in rLV-CON group, particularly in pathways such as G-protein coupled receptor (GPCR) downstream signaling and signaling by GPCR (Fig. 3J). Finally, the expression level of *RPL26* was significantly increased in the rLV-*RAB11B-AS1* group compared with rLV-CON group (Fig. 3K). Collectively, these observations suggest that *RAB11B-AS1* enhances the transcriptional ability of *RPL26*.

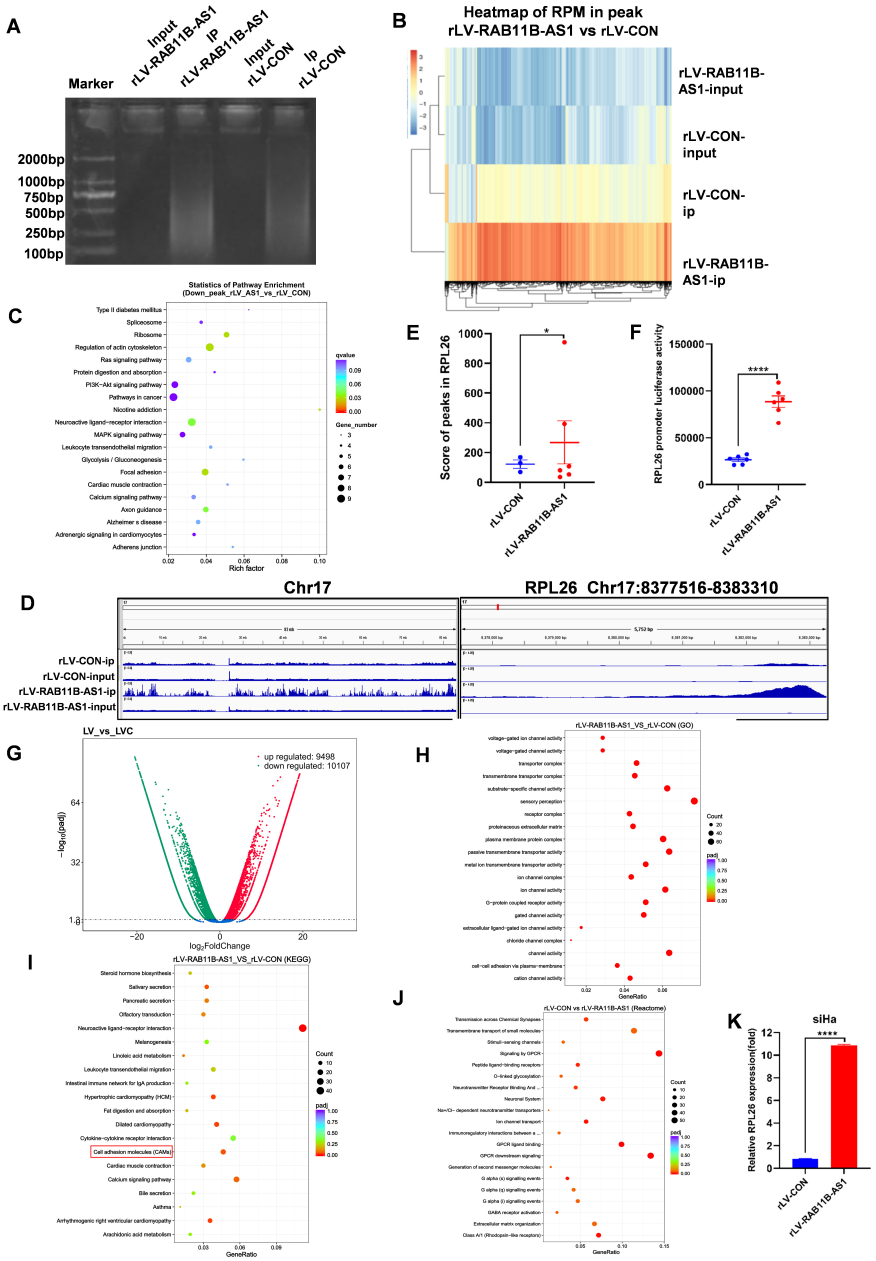

Fig. 3. *RAB11B-AS1* enhances the transcriptional activity of *RPL26* by the modification of H3K9ac. (A) IP enriched *RAB11B-AS1* content in the rLV-CON and rLV-*RAB11B-AS1* groups. (B) Heat map of RPM in peaks in the rLV-*RAB11B-AS1* and rLV-CON groups. (C) KEGG enrichment analysis of down-regulated genes after *RAB11B-AS1* overexpression in ChIP-seq data. (D) Different modification ability of H3K9ac on chromosome 17 was visually browsed using the IGV browser. H3K9ac data indicated enhanced transcriptional activity of *RPL26* in the rLV-*RAB11B-AS1* and rLV-CON groups. (E) Analysis of the score of peaks in *RPL26* between the rLV-*RAB11B-AS1* and rLV-CON groups. (F) Analysis of *RPL26* promoter luciferase activity between the rLV-*RAB11B-AS1* and rLV-CON group. (G) Volcano plot of differential transcripts. Abscissa presents log2FC and ordinate presents-log10 (padj). (H) The transcriptomics GO enrichment analysis is illustrated in a scatter plot, where the GeneRatio is plotted against GO term annotations. Dot color represents the adjusted *p*-value (padj), and dot size corresponds to the number of enriched transcripts. (I) KEGG pathway enrichment analysis of up-regulated differential genes after *RAB11B-AS1* overexpression in RNA-seq results. (J) Analysis of reactome pathway enrichment. Log10 (padj) and ordinate present reactome pathway enrichment annotation and the number of enriched transcripts. (K) qRT-PCR showed that *RPL26* was significantly up-regulated after *RAB11B-AS1* overexpression. For (E,F,K) Data represent the mean ± s.d., and statistical analyses were performed using two-tailed unpaired *t*-tests. ChIP-seq, Chromatin immunoprecipitation sequencing; *RPL26*, ribosomal protein L26. *, $p \leq 0.05$; ****, $p \leq 0.0001$.

3.4 RAB11B-AS1 Up-Regulates the Protein Expression of RPL26

Considering that *RAB11B-AS1* can alter cancer related-genes at the level of transcription, we determined whether *RAB11B-AS1* regulates cancer related genes at the protein level. Proteins were isolated from cells infected by rLV-*RAB11B-AS1* and rLV-CON, followed by quantitative analysis. A volcano plot revealed 97 differentially expressed proteins (DEPs) out of a total of 6536 identified proteins. This subset, included 51 upregulated and 46 downregulated proteins in the rLV-*RAB11B-AS1* group compared with the rLV-CON group, such as *RPL26*, S100A14, EML2, CRABP2, TMEM168, MAP2, RPS23, and RPL37 (Fig. 4A). Subcellular localization analysis revealed that the DEPs were mainly enriched in the nucleus (34.92%) (Fig. 4B). GO analysis showed that the DEPs were highly enriched in the rLV-*RAB11B-AS1* group compared to in rLV-CON group, including protein phosphorylation (n = 199), metabolic process (n = 126), nucleus (n = 307), integral component of membrane (n = 199), protein binding (n = 1201), ATP binding (n = 527), and zinc ion binding (n = 339) (Fig. 4C). Proteomics KEGG analysis showed that the DEPs were highly enriched in rLV-*RAB11B-AS1* group, including systemic lupus erythematosus, cardiac muscle contraction and hypertrophic cardiomyopathy. In particular, the differentially expressed transcripts were highly enriched in the ribosome in the rLV-*RAB11B-AS1* group compared with the rLV-CON group (Fig. 4D). Protein-protein interactions analysis showed that 103 upregulated proteins (e.g., *RPL26*, MAP2, RPL28, RPL37) and 53 downregulated proteins involved in the protein were interaction network (e.g., S100A14, EML2, CRABP2, TMEM168) (Fig. 4E–G). Among these, the most pronounced variation was observed in *RPL26* expression. Subsequent validation by western blotting revealed a significant reduction in *RPL26* protein levels following *RAB11B-AS1* knockout (Fig. 4H).

3.5 RAB11B-AS1 Regulates the Expression of Cancer Related-Genes by Enhancing RPL26

To further elucidate the downstream mechanism by which *RAB11B-AS1* modulates CC progression via *RPL26*, we transduced *RAB11B-AS1*-overexpressing cells with *RPL26*-targeting shRNA; western-blot analysis confirmed efficient knockdown (Fig. 5A). Volcano-plot comparison of rLV-CON versus rLV-*RAB11B-AS1*+rLV-shRNA-*RPL26* revealed 320 up-regulated genes (including S100A14, EML2, CRABP2 and TMEM168) and 725 down-regulated genes (including MAP2) (Fig. 5B). Gene Ontology enrichment analyses identified receptor-regulator activity, peptide binding and transmembrane-signaling-receptor activity as significantly enriched among the up-regulated genes in the rLV-*RAB11B-AS1* group, yet these same categories were conversely enriched among the down-regulated genes in the rLV-*RAB11B-AS1*+rLV-shRNA-*RPL26* group (Fig. 5C,D). KEGG pathway mapping further demonstrated that Pentose and glucuronate interconversions, cell adhesion molecules (CAMs), JAK-STAT signaling and cytokine–cytokine receptor interaction were up-regulated in rLV-*RAB11B-AS1* cells but significantly down-regulated upon *RPL26* silencing (Fig. 5E,F).

To further validate the above findings, we performed a proteomic analysis. Volcano plot analysis identified a total of 505 DEPs, including 209 upregulated proteins and 397 downregulated proteins in the rLV-*RAB11B-AS1* group compared with the rLV-CON group. A total of 415 DEPs were identified, including 214 upregulated proteins and 201 downregulated proteins in the rLV-*RAB11B-AS1*+ rLV-shRNA-*RPL26* group compared with the rLV-CON group (Fig. 5G,H). Proteomics GO analysis showed that the DEPs in the rLV-*RAB11B-AS1* group exhibited significant enrichment in several terms-including dephosphorylation compared to the rLV-CON group. Conversely, the GO terms, cell junction, dephosphorylation were not enriched in the rLV-*RAB11B-AS1*+rLV-shRNA-*RPL26* group compared with the rLV-CON group (Fig. 5I,J). Proteomics KEGG analysis showed that the DEPs were highly enriched in rLV-*RAB11B-AS1* group compared to the rLV-CON group, including phagosome, Hedgehog signaling pathway, and inositol phosphate metabolism. These KEGG terms, were not enriched in the rLV-*RAB11B-AS1*+rLV-shRNA-*RPL26* group compared with the rLV-CON group (Fig. 5K,L). Collectively, these observations suggest that *RAB11B-AS1* regulates the expression of cancer related-genes by enhancing *RPL26*.

3.6 RPL26 Knockdown Abrogates the Suppressor Function of RAB11B-AS1 In Vivo

To explore the effect of *RPL26* on *RAB11B-AS1* overexpression inhibiting CC, we performed *in vitro* and *in vivo* experiments. CCK-8 assays showed that compared with the rLV-CON group, the proliferation ability was significantly decreased in the rLV-*RAB11B-AS1* group; however, the proliferation ability was significantly increased in the rLV-*RAB11B-AS1*+rLV-shRNA-*RPL26* group (Fig. 6A). Furthermore, compared with the rLV-CON group, the colony formation rate was notably decreased in the rLV-*RAB11B-AS1* group, but was notably increased in the rLV-*RAB11B-AS1*+ rLV-shRNA-*RPL26* group (Fig. 6B). Next, tumorigenesis test *in vivo* was performed in nude mice. Compared with the rLV-CON group, the average weight of xenograft tumors was significantly decreased in the rLV-*RAB11B-AS1* group. However, compared with the rLV-*RAB11B-AS1* group, the average weight of xenograft tumors was remarkably increased in the rLV-*RAB11B-AS1*+rLV-shRNA-*RPL26* group (Fig. 6C,D). Tumor onset time was significantly increased in the rLV-*RAB11B-AS1* group compared with the rLV-CON group. However, compared with the rLV-*RAB11B-AS1* group, the appearance time of xenograft tumors was significantly shortened in the rLV-*RAB11B-AS1*+ rLV-shRNA-*RPL26* group (Fig. 6E). H&E staining

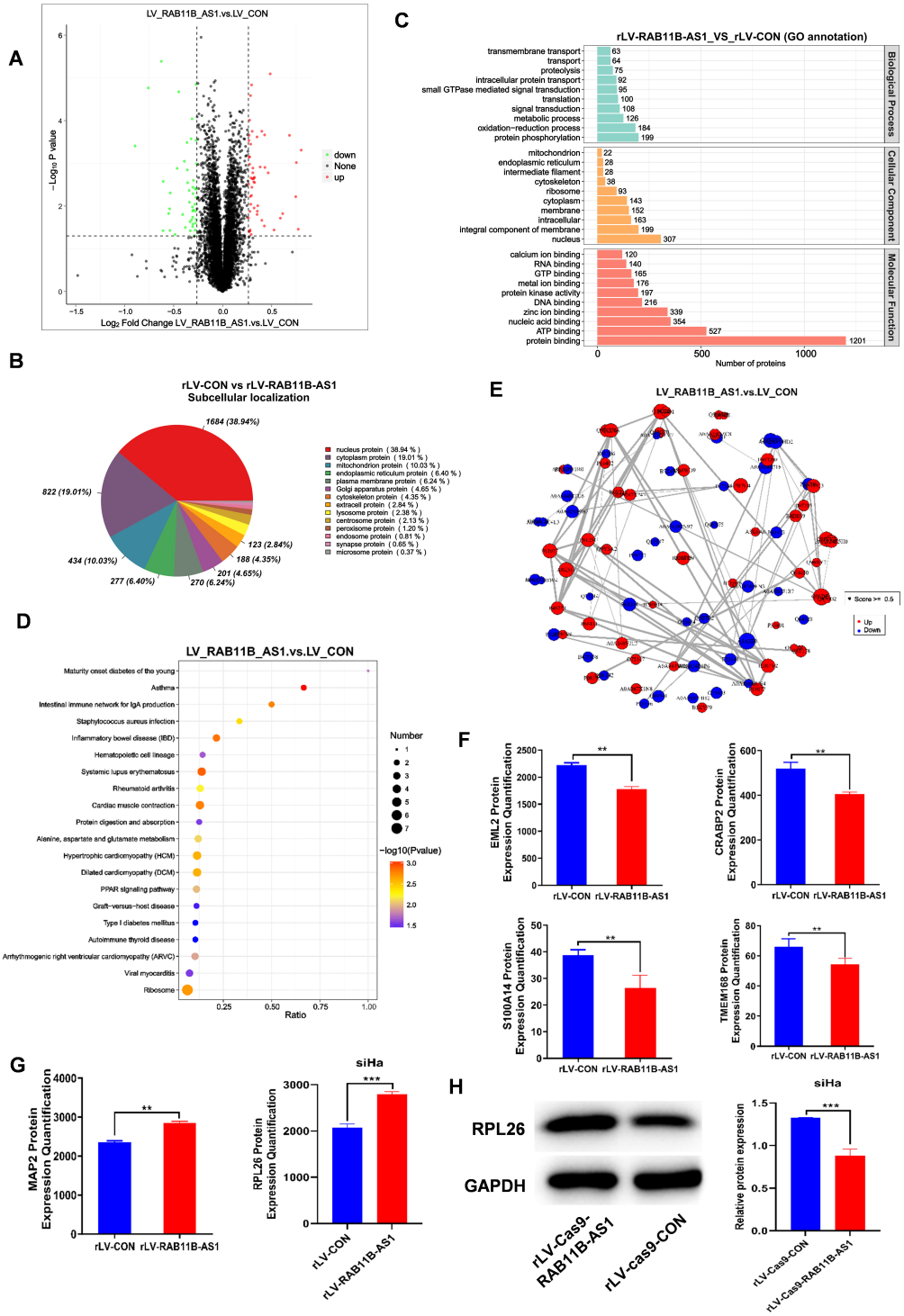

Fig. 4. *RAB11B-AS1* up-regulates the protein expression of RPL26. (A) Volcano plots of DEPs in the rLV-*RAB11B-AS1* and rLV-CON groups. (B) Subcellular localization of DEPs. (C) Analysis of proteomics GO enrichment. Abscissa presents the number of enriched proteins and the ordinate presents the GO enrichment annotation. (D) Scatter diagram of proteomics KEGG enrichment. Abscissa presents the Ratio and the ordinate presents KEGG enrichment items. (E) Protein-protein interaction networks. Red presents upregulated proteins and blue present downregulated proteins. (F,G) Tandem mass tag labeled protein quantification analysis was performed in SiHa infected with rLV-*RAB11B-AS1* and rLV-CON. (H) *RPL26* was detected by Western blot analysis using antibodies against *RPL26* with actin as a loading control. All measurement data are expressed as mean ± SD. For (F–H) Data represent the mean ± s.d., and statistical analyses were performed using two-tailed unpaired *t*-tests. DEPs, differentially expressed proteins. **, $p \leq 0.01$; ***, $p \leq 0.001$.

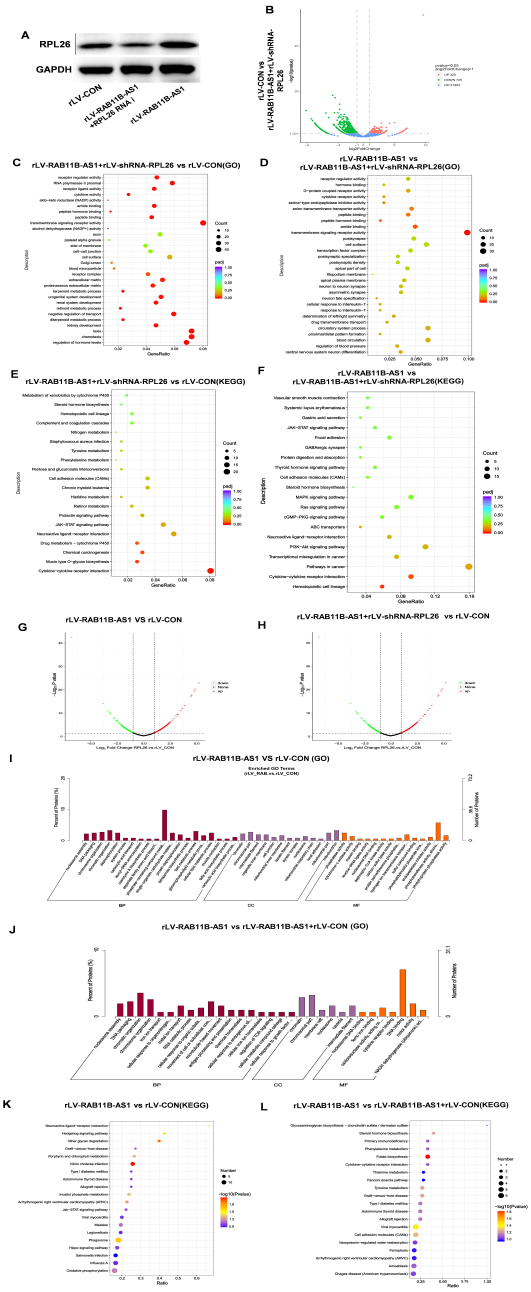

Fig. 5. *RAB11B-AS1* regulates the expression of cancer related-genes by enhancing *RPL26*. (A) Western blot analysis was used to detect the efficiency of *RPL26* knockdown based on *RAB11B-AS1* overexpression. (B) Volcano plot of differentially expressed transcripts between the rLV-CON group and the rLV-*RAB11B-AS1* + rLV-shRNA-*RPL26* group. (C) Scatter plot of transcriptomic GO enrichment analysis comparing the rLV-CON group and the rLV-*RAB11B-AS1* + rLV-shRNA-*RPL26* group group. (D) Scatter plot of transcriptomic GO enrichment analysis comparing the rLV-*RAB11B-AS1* group and the rLV-*RAB11B-AS1* + rLV-shRNA-*RPL26* group group. (E) KEGG pathway enrichment analysis of differentially expressed genes between the rLV-CON group and the rLV-*RAB11B-AS1* + rLV-shRNA-*RPL26* group group. (F) KEGG pathway enrichment analysis of differentially expressed genes between the rLV-*RAB11B-AS1* group and the rLV-*RAB11B-AS1* + rLV-shRNA-*RPL26* group. (G) Volcano plot displaying differentially expressed transcripts between the rLV-CON group and the rLV-*RAB11B-AS1* group. The x-axis represents $\log_2$(fold change), and the y-axis represents –log10 (*p* value). (H) Volcano plot of differentially expressed transcripts between the rLV-CON group and the rLV-*RAB11B-AS1* + rLV-shRNA-*RPL26* group. (I) Scatter plot of proteomic GO enrichment analysis comparing the rLV-CON group and the rLV-*RAB11B-AS1* group. (J) Scatter plot of proteomic GO enrichment analysis comparing the rLV-CON group and the rLV-*RAB11B-AS1* + rLV-shRNA-*RPL26* group. The x axis shows the GO term annotations, and the y axis indicates the number of enriched proteins. (K) Scatter plot of proteomic KEGG pathway enrichment analysis between the rLV-CON group and the rLV-*RAB11B-AS1* group. (L) Scatter plot of proteomic KEGG pathway enrichment analysis between the rLV-CON group and the rLV-*RAB11B-AS1* + rLV-shRNA-*RPL26* group.

showed that poorly differentiated cells were significantly decreased in the rLV-*RAB11B-AS1* group compared with the rLV-CON group but markedly increased in the rLV-*RAB11B-AS1*+ rLV-shRNA-*RPL26* group compared with the rLV-CON group (Fig. 6F,G). Compared with the rLV-CON group, PCNA positivity rate was significantly decreased in the rLV-*RAB11B-AS1* group. However, compared with therLV-*RAB11B-AS1* group, the PCNA positive rate was significantly increased in the rLV-*RAB11B-AS1*+rLV-shRNA-*RPL26* group (Fig. 6F,H).

4. Discussion

Globally, CC is the second most frequent cause of death among women aged between the ages of 20 and 39 years [12]. 5-year overall survival rate of patients with locally advanced CC is less than 70% [4]. Recently, although great progress has been made in the diagnosis and treatment of human CC, the precise mechanisms of cervical carcinogenesis remain largely unknown and require further study. This study clearly showed that *RAB11B-AS1* can inhibit the progression of CC through the regulation of cancer-related pathways based on ribosomal proteins, cell cycle and CAMs among others (Fig. 6I). These findings provide basic data for the study of human CC.

A growing body of research indicates that various oncogenic or tumor-suppressive lncRNAs in cervical cancer function as competitive endogenous RNAs (ceRNAs), sequestering specific miRNAs and thereby relieving repression on downstream target genes. This regulatory mode ultimately alters key malignant phenotypes, including cell-cycle progression, EMT, and metastatic potential [13]. For example, HIF1A-AS2 has been shown to act as a molecular sponge for miR-34b-5p, enhances cervical cancer cell proliferation and invasion while suppressing apoptosis [14]. Therefore, further elucidation of lncRNA-mediated regulatory mechanisms in cervical cancer is of substantial clinical significance and may provide new avenues for biomarker development and targeted therapy. The present study demonstrated a decreased expression of *RAB11B-AS1* in cervical cancer specimens versus matched para-cancerous tissues, which was inversely correlated with pathological grade of human CC. Notably, our results suggest that *RAB11B-AS1* reduced the growth ability, increases apoptosis, and inhibits cell migration in human cervical cancer cells. Disrupting calcium-dependent energy metabolism leads to apoptosis in Triple-negative breast cancer (TNBC) cells [15] . Especially, inducing apoptosis is the main goal of cancer therapy [16]. In this study, excessive *RAB11B-AS1* promotes both early and late apoptosis. These findings align with existing reports, suggesting that *RAB11B-AS1* likely suppresses CC by inducing apoptosis.

In particular, our results demonstrate that *RAB11B-AS1* was negatively correlated with CC metastasis. Cell-cell adhesion and the extracellular matrix are well-known determinants of cancer invasion and metastasis [17]. Moreover, EMT-mediated migration promotes cancer progression [18]. Thus, we postulate that *RAB11B-AS1* inhibit the CC migration and invasion by changing cell-cell junctions or the EMT. Intriguingly, our results suggest that *RAB11B-AS1* regulates several cancer related-genes in CC. Studies indicate that *RPL26* is the main target of ubiquitin fold modifier 1 conjugation, which is a ribosomal modification [19]. UFMylation of *RPL26* is associated with endoplasmic reticulum protein homeostasis [20]. Reports suggest that *RPL26* is a p53 regulator and increases p53 expression [21–23] by inhibiting the activity of HDM2 [24] and Mdm2 [25]. Studies have demonstrated that MAP2 plays a pivotal role in the neurite outgrowth of neuronal cells [26] and negatively regulates tumorigenesis [27]. The antitumor functions of RAB11B-AS1, such as inhibiting cell proliferation, migration, and invasion of CC cells [28], may be linked to its ability to increase the expression of MAP2, which is itself a known inhibitor of these cellular processes [27].

Studies have shown that the proteins echinoderm microtubule-associated protein-like-2, endothelial monocyte-activating protein 2 (EMAPII) regulate tumorigenesis [29]. In our study, we found that *RAB11B-AS1* inhibited the expression of EMAPII leading us to postulate that *RAB11B-AS1* inhibits CC growth through a separate function of EMAPII, which requires further investigation. Study indicates that CRABP2 is a cellular binding-protein and, an intracellular retinoic acid transporter [30]. Reports suggest that altered CRABP2 expression promotes more severe outcomes in several cancers [31] and regulates breast cancer invasion dependent on its ER status [32]. These data suggest that *RAB11B-AS1* may block the progression of CC by inhibiting CRABP2. S100A14 is involved in cell proliferation, cell differentiation and tumor metastasis [33]. In particular, S100A14 promotes cell proliferation by altering the cellular G2/M phase, migration and invasion in CC [34], suggesting that *RAB11B-AS1* may affect these signaling pathways by reducing S100A14 expression in CC. Consequently, *RAB11B-AS1* regulation of key proteins, including *RPL26*, EML2, CRABP2, TMEM168, MAP2, and S100A14 is critical for inhibiting cervical carcinogenesis.

In HeLa cells, the G1/S checkpoint has been shown to be regulated by miRNAs [35]. Strikingly, our results showed that *RAB11B-AS1* affects cancer-related pathways related to ribosomal proteins, cell cycle and CAMs. *RAB11B-AS1* also regulates cancer metastasis-related adhesion junction signaling pathways by altering actin. Our study indicates that *RAB11B-AS1* inhibits CC metastasis potentially through its involvement in cell-cell adhesion. This aligns with research indicating that the ability of cancer to invade and metastasize is tied to cell adhesion properties [36]. In particular, our results showed that *RAB11B-AS1* also affects important cancer pathways by upregulating HO-1, plakoglobin, and GSTs, and downregulating TRK. The study reveals that HO-1 exerts anti-inflammatory and

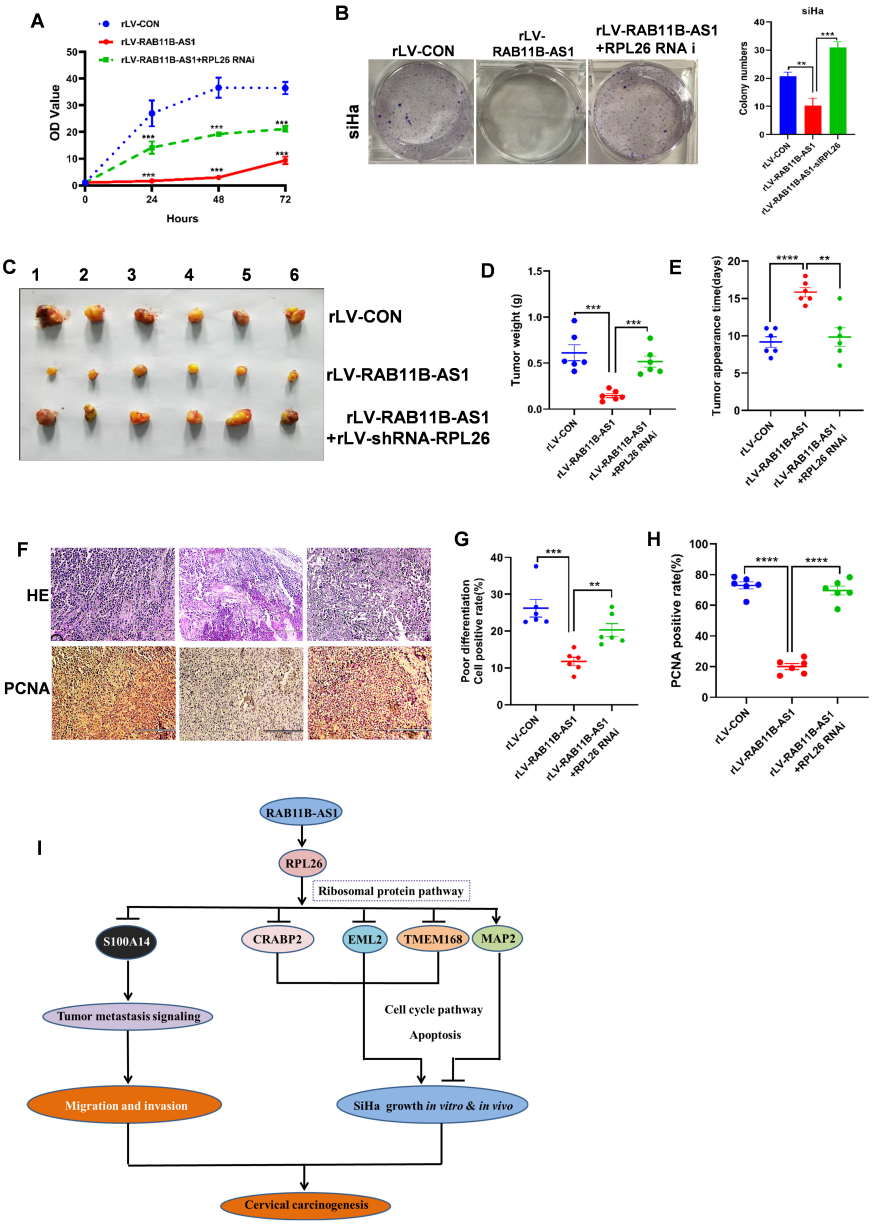

Fig. 6. *RPL26* knockdown abrogates the suppressor function of *RAB11B-AS1 in vivo*. (A) CCK-8 assay was used to detect the proliferation trend of rLV-CON, rLV-*RAB11B-AS1* and rLV-*RAB11B-AS1*+rLV-shRNA-*RPL26* groups. (B) Cell colony formation ability in the rLV-CON, rLV-*RAB11B-AS1*, and rLV-*RAB11B-AS1*-rLV-shRNA-*RPL26* groups. Representative images from three independent biological replicates are shown. (C) The nude mice were euthanized at 30 days and the transplanted tumors were imaged, including the rLV-CON, rLV-*RAB11B-AS1* and rLV-*RAB11B-AS1*-rLV-shRNA-*RPL26* group. (D) Comparison of average xenograft tumor weight among the rLV-CON, rLV-*RAB11B-AS1* and rLV-*RAB11B-AS1*-rLV-shRNA-*RPL26* group. (E) Comparison of appearance time (days) of xenograft tumor among the rLV-CON, rLV-*RAB11B-AS1* and rLV-*RAB11B-AS1*-rLV-shRNA-*RPL26* groups. (F) H&E staining and immunohistochemistry with anti-PCNA from xenograft tumor among the rLV-CON, rLV-*RAB11B-AS1* and rLV-*RAB11B-AS1*-rLV-shRNA-*RPL26* groups. The picture of H&E staining (upper) and immunohistochemistry with anti-PCNA (lower); scale bar, 200 μm. (G) Analysis of H&E staining cell positive rate (%) from xenograft tumor among the rLV-CON, rLV-*RAB11B-AS1* and rLV-*RAB11B-AS1*-rLV-shRNA-*RPL26* groups. (H) Analysis of PCNA positive rate (%) from xenograft tumor among the rLV-CON, rLV-*RAB11B-AS1* and rLV-*RAB11B-AS1*-rLV-shRNA-*RPL26* groups. (I) Schematic diagram illustrating the mechanism by which RAB11B-AS1 inhibits cervical cancer progression through the regulation of ribosomal proteins, cell cycle, and adhesion molecule-related pathways. All quantitative data are presented as mean ± SD. For A statistical analyses were performed using one-way ANOVA tests. For (B,D,E,G,H) data represent the mean ± s.d., and statistical analyses were performed using two-tailed unpaired *t*-tests. **, $p \leq 0.01$; ***, $p \leq 0.001$; ****, $p \leq 0.0001$.

cytoprotective effects by regulating p53/Mdm2 signaling axis [37]. Plakoglobin is highly differentially expressed in breast cancer and contributes to breast cancer metastasis [38]. GSTs are a superfamily of enzymes that can conjugate glutathione [39] and are involved in cancer cell growth and differentiation [40]. TRK pathway aberrations are involved in the pathogenesis of many cancer types [41–43]. Taken together, our study found that *RAB11B-AS1* promoted apoptosis and inhibited proliferation and metastasis through *RPL26*-mediated p53 pathway.

While this study provides initial insights into the oncogenic role of the long non-coding RNA RAB11B-AS1 in cervical cancer, several limitations merit consideration. First, functional assays were restricted to a single cervical cancer cell line (SiHa); thus, the generalizability of our findings remains to be validated in additional models. Second, potential off-target effects cannot be excluded, necessitating further investigation to strengthen the clinical relevance of our observations. Third, downstream mechanisms of RAB11B-AS1 were inferred solely from transcriptomic profiling, without experimental validation.

5. Conclusions

To summarize, our findings demonstrate that *RAB11B-AS1* suppresses the progression of human CC by regulating key the cancer-related pathways involving ribosomal proteins, cell-cycle regulation, and CAMs. Specifically, *RPL26* plays a key role for *RAB11B-AS1* exerts its effects in human CC. These results offer crucial foundational data that could inform future strategies for CC treatment.

Availability of Data and Materials

The datasets used and analyzed during the current study are available from the corresponding author upon reasonable request.

Author Contributions

XT and YOY conceived the study and participated in the study design, performance, coordination, and manuscript writing. XG, YY, ZZ performed the research. All authors contributed to editorial changes in the manuscript. All authors read and approved the final manuscript. All authors have participated sufficiently in the work and agreed to be accountable for all aspects of the work.

Ethics Approval and Consent to Participate

All procedures related to patients were carried out in accordance with International Ethical Guidelines for Biomedical Research Involving Human Subjects (CIOMS). The studies were approved by the Ethics Committee of Shanghai Tongji Hospital (Approval Number: K-W-2025-011). This study was conducted in accordance with the guiding principles of the Declaration of Helsinki. All the mouse experiments were approved by the Animal Ethics Committee of Tongji University (Approval Number: TJAB04225102). The housing of the mice was conducted in accordance with the guidelines stipulated by the National Institutes of Health (NIH) Guide for the Care and Use of Laboratory Animals (NIH Publication No. 8023, revised 1978). The patients/participants provided their written informed consent to participate in this study.

Acknowledgment

Not applicable.

Funding

This study was supported by a grant from the National Natural Science Foundation of China (NCSF no.81974404) and (NCSF no.81702745).

Conflict of Interest

The authors declare no conflict of interest.

References

[1] Siegel RL, Miller KD, Jemal A. Cancer statistics, 2020. CA: A Cancer Journal for Clinicians. 2020; 70: 7–30. https://doi.org/10.3322/caac.21590.

[2] Bray F, Ferlay J, Soerjomataram I, Siegel RL, Torre LA, Jemal A. Global cancer statistics 2018: GLOBOCAN estimates of incidence and mortality worldwide for 36 cancers in 185 countries. CA: A Cancer Journal for Clinicians. 2018; 68: 394–424. https://doi.org/10.3322/caac.21492.

[3] Wei W, Zeng H, Zheng R, Zhang S, An L, Chen R, *et al*. Cancer registration in China and its role in cancer prevention and control. The Lancet Oncology. 2020; 21: e342–e349. https://doi.org/10.1016/S1470-2045(20)30073-5.

[4] Cohen PA, Jhingran A, Oaknin A, Denny L. Cervical cancer. The Lancet. 2019; 393: 169–182. https://doi.org/10.1016/S0140-6736(18)32470-X.

[5] Statello L, Guo CJ, Chen LL, Huarte M. Gene regulation by long non-coding RNAs and its biological functions. Nature Reviews Molecular Cell Biology. 2021; 22: 96–118. https://doi.org/10.1038/s41580-020-00315-9.

[6] Dong J, Su M, Chang W, Zhang K, Wu S, Xu T. Long non-coding RNAs on the stage of cervical cancer. Oncology Reports. 2017; 38: 1923–1931. https://doi.org/10.3892/or.2017.5879.

[7] Wang D, Hu X, Chen J, Liang B, Zhang L, Qin P, *et al*. Bioinformatics Analysis and Validation of the Role of Lnc-RAB11B-AS1 in the Development and Prognosis of Hepatocellular Carcinoma. Cells. 2022; 11: 3517. https://doi.org/10.3390/cells11213517.

[8] Chen Z, Liu Z, Yang Y, Zhu Z, Liang R, Huang B, *et al*. Long non-coding RNA RAB11B-AS1 prevents osteosarcoma development and progression via its natural antisense transcript RAB11B. Oncotarget. 2018; 9: 26770–26786. https://doi.org/10.18632/oncotarget.25484.

[9] Li T, Wu D, Liu Q, Wang D, Chen J, Zhao H, *et al*. Upregulation of long noncoding RNA RAB11B-AS1 promotes tumor metastasis and predicts poor prognosis in lung cancer. Annals of Translational Medicine. 2020; 8: 582–582. https://doi.org/10.21037/atm-20-3021.

[10] Niu Y, Bao L, Chen Y, Wang C, Luo M, Zhang B, *et al*. HIF2-induced long noncoding RNA RAB11B-AS1 promotes hypoxia-mediated angiogenesis and breast cancer metastasis. Cancer Re-

search. 2020; 80: 964–975. https://doi.org/10.1158/0008-5472.CAN-19-1718.
[11] Dai YZ, Liu YD, Li J, Chen MT, Huang M, Wang F, *et al*. METTL16 promotes hepatocellular carcinoma progression through downregulating RAB11B-AS1 in an m6A-dependent manner. Cellular and Molecular Biology Letters. 2022; 27: 41–41. https://doi.org/10.1186/s11658-022-00343-5.
[12] Siegel RL, Miller KD, Jemal A. Cancer statistics, 2019. CA: A Cancer Journal for Clinicians. 2019; 69: 7–34. https://doi.org/10.3322/caac.21551.
[13] Xu Y, Sun Y, Song X, Ren J. The mechanisms and diagnostic potential of lncRNAs, miRNAs, and their related signaling pathways in cervical cancer. Frontiers in Cell and Developmental Biology. 2023; 11: 1170059–1170059. https://doi.org/10.3389/fcell.2023.1170059.
[14] Liu Y, Zhang Y, Chen C, Roy B, Li Q, Zhang W, *et al*. lncRNA HIF1A-AS2 acts as an oncogene to regulate malignant phenotypes in cervical cancer. Frontiers in Oncology. 2025; 15: 1530677–1530677. https://doi.org/10.3389/fonc.2025.1530677.
[15] Liao C, Zhang Y, Fan C, Herring LE, Liu J, Locasale JW, *et al*. Identification of BBOX1 as a therapeutic target in triple-negative breast cancer. Cancer Discovery. 2020; 10: 1706–1721. https://doi.org/10.1158/2159-8290.CD-20-0364.
[16] Carneiro BA, El-Deiry WS. Targeting apoptosis in cancer therapy. Nature Reviews Clinical Oncology. 2020; 17: 395–417. https://doi.org/10.1038/s41571-020-0341-y.
[17] Ilina O, Gritsenko PG, Syga S, Lippoldt J, La Porta CAM, Chepizhko O, *et al*. Cell-cell adhesion and 3D matrix confinement determine jamming transitions in breast cancer invasion. Nature Cell Biology. 2020; 22: 1103–1115. https://doi.org/10.1038/s41556-020-0563-1.
[18] Li CF, Chen JY, Ho YH, Hsu WH, Wu LC, Lan HY, *et al*. Snail-induced claudin-11 prompts collective migration for tumour progression. Nature Cell Biology. 2019; 21: 251–262. https://doi.org/10.1038/s41556-018-0268-z.
[19] Walczak CP, Leto DE, Zhang L, Riepe C, Muller RY, DaRosa PA, *et al*. Ribosomal protein RPL26 is the principal target of UFMylation. Proceedings of the National Academy of Sciences of the United States of America. 2019; 116: 1299–1308. https://doi.org/10.1073/pnas.1817305116.
[20] Wang L, Xu Y, Rogers H, Saidi L, Noguchi CT, Li H, *et al*. UFMylation of RPL26 links translocation-associated quality control to endoplasmic reticulum protein homeostasis. Cell Research. 2020; 30: 5–20. https://doi.org/10.1038/s41422-019-0259-3.
[21] Gazda HT, Preti M, Sheen MR, O'Donohue MF, Vlachos A, Davies SM, *et al*. Frameshift mutation in p53 regulator RPL26 is associated with multiple physical abnormalities and a specific pre-ribosomal RNA processing defect in Diamond-Blackfan anemia. Human Mutation. 2012; 33: 1037–1044. https://doi.org/10.1002/humu.22080.
[22] Chen J, Guo K, Kastan MB. Interactions of nucleolin and ribosomal protein L26 in translational control of human p53 mRNA. Journal of Biological Chemistry. 2012; 287: 16467–16476. https://doi.org/10.1074/jbc.M112.350306.
[23] Takagi M, Absalon MJ, McLure KG, Kastan MB. Regulation of p53 translation and induction after DNA damage by ribosomal protein L26 and nucleolin. Cell. 2005; 123: 49–63. https://doi.org/10.1016/j.cell.2005.07.034.
[24] Zhang Y, Wang J, Yuan Y, Zhang W, Guan W, Wu Z, *et al*. Negative regulation of HDM2 to attenuate p53 degradation by ribosomal protein L26. Nucleic Acids Research. 2010; 38: 6544–6554. https://doi.org/10.1093/nar/gkq536.
[25] Ofir-Rosenfeld Y, Boggs K, Michael D, Kastan MB, Oren M. Mdm2 regulates p53 mRNA translation through inhibitory interactions with ribosomal protein L26. Molecular Cell. 2008; 32: 180–189. https://doi.org/10.1016/j.molcel.2008.08.031.
[26] Liu SY, Chen YT, Tseng MY, Hung CC, Chiang WF, Chen HR, *et al*. Involvement of microtubule-associated protein 2 in oral cancer cell motility. Biochemical and Biophysical Research Communications. 2008; 366: 520–525. https://doi.org/10.1016/j.bbrc.2007.12.017.
[27] Zhao HD, Ma Y, Wu XS, Cheng JJ, Xia ZG, Kan C, *et al*. Circ_001680 aggravates the malignant process of gastric carcinoma by targeting MAP2. European Review for Medical and Pharmacological Sciences. 2020; 24: 6072–6079. https://doi.org/10.26355/eurrev_202006_21569.
[28] Córdova-Rivas S, Fraire-Soto I, Mercado-Casas Torres A, Servín-González LS, Granados-López AJ, López-Hernández Y, *et al*. 5p and 3p strands of miR-34 family members have differential effects in cervical cancer cells. International Journal of Molecular Sciences. 2019; 20: 1180–1180. https://doi.org/10.3390/ijms20031180.
[29] Zhou Z, Sun B, Huang S, Yu D, Zhang X. Roles of aminoacyl-tRNA synthetase-interacting multifunctional proteins in physiology and cancer. Cell Death and Disease. 2020; 11: 579–579. https://doi.org/10.1038/s41419-020-02832-3.
[30] Napoli JL, Yoo HS. Retinoid metabolism and functions mediated by retinoid binding proteins. Methods in Enzymology. 2020; 637: 55–75. https://doi.org/10.1016/bs.mie.2020.02.001.
[31] Napoli JL. Cellular retinoid binding-proteins CRBP, CRABP, FABP5: effects on retinoid metabolism, function and related diseases. Pharmacology and Therapeutics. 2017; 173: 19–33. https://doi.org/10.1016/j.pharmthera.2017.01.004.
[32] Feng X, Zhang M, Wang B, Zhou C, Mu Y, Li J, *et al*. CRABP2 regulates invasion and metastasis of breast cancer through Hippo pathway dependent on ER status. Journal of Experimental and Clinical Cancer Research. 2019; 38: 361–361. https://doi.org/10.1186/s13046-019-1374-5.
[33] Zhu M, Wang H, Cui J, Li W, An G, Pan Y, *et al*. Calcium-binding protein S100A14 induces differentiation and suppresses metastasis in gastric cancer. Cell Death and Disease. 2017; 8: e2938–e2938. https://doi.org/10.1038/cddis.2017.336.
[34] Wang X, Yang J, Qian J, Liu Z, Chen H, Cui Z. S100A14 regulates proliferation, migration and invasion of human cervical cancer cells. American Journal of Cancer Research. 2015; 5: 1484–1495.
[35] Gupta S, Panda PK, Hashimoto RF, Samal SK, Mishra S, Verma SK, *et al*. Dynamical modeling of miR-34a, miR-449a and miR-16 reveals DDR signaling pathways in HeLa cells. Scientific Reports. 2022; 12: 4911–4911. https://doi.org/10.1038/s41598-022-08952-0.
[36] Dhar D, Antonucci L, Nakagawa H, Kim JY, Glitzner E, Caruso S, *et al*. Liver cancer initiation requires p53 inhibition by CD44-enhanced growth factor signaling. Cancer Cell. 2018; 33: 1061–1077. https://doi.org/10.1016/j.ccell.2018.05.003.
[37] Nakamura K, Zhang M, Kageyama S, Ke B, Fujii T, Sosa RA, *et al*. Macrophage heme oxygenase-1-SIRT1-p53 axis regulates sterile inflammation in liver ischemia-reperfusion injury. Journal of Hepatology. 2017; 67: 1232–1242. https://doi.org/10.1016/j.jhep.2017.08.003.
[38] Aceto N, Bardia A, Miyamoto DT, Donaldson MC, Wittner BS, Spencer JA, *et al*. Circulating tumor cell clusters are oligoclonal precursors of breast cancer metastasis. Cell. 2014; 158: 1110–1122. https://doi.org/10.1016/j.cell.2014.07.013.
[39] Tsuboi K, Bachovchin DA, Speers AE, Spicer TP, Fernandez-Vega V, Hodder P, *et al*. Potent and selective inhibitors of glutathione S-transferase omega 1 that impair cancer drug resistance. Journal of the American Chemical Society. 2011; 133: 16605–16616. https://doi.org/10.1021/ja207218n.
[40] Laborde E. Glutathione transferases as mediators of signaling pathways involved in cell proliferation and cell death. Cell Death

and Differentiation. 2010; 17: 1373–1380. https://doi.org/10.1038/cdd.2010.80.
[41] Amatu A, Sartore-Bianchi A, Bencardino K, Pizzutilo EG, Tosi F, Siena S. Tropomyosin receptor kinase biology and the role of NTRK gene fusions in cancer. Annals of Oncology. 2019; 30: viii5–viii15. https://doi.org/10.1093/annonc/mdz383.
[42] Khotskaya YB, Holla VR, Farago AF, Mills Shaw KR, Meric-Bernstam F, Hong DS. Targeting TRK family proteins in cancer. Pharmacology and Therapeutics. 2017; 173: 58–66. https://doi.org/10.1016/j.pharmthera.2017.02.006.
[43] Doebele RC. Acquired resistance is oncogene and drug agnostic. Cancer Cell. 2019; 36: 347–349. https://doi.org/10.1016/j.ccell.2019.09.011.